

# THE SWIFT X-RAY TELESCOPE

David N. Burrows, J. E. Hill, J. A. Nousek and J. A. Kennea  
*Pennsylvania State University, 525 Davey Lab, University Park, PA 16802, USA*  
 (burrows@astro.psu.edu)

A. Wells, J. P. Osborne, A. F. Abbey, A. Beardmore, K. Mukerjee  
 and A.D.T. Short  
*Space Research Centre, University of Leicester, Leicester LE1 7RH, UK*

G. Chincarini, S. Campana, O. Citterio, A. Moretti, C. Pagani and G.  
 Tagliaferri  
*INAF-Osservatorio Astronomico di Brera, Via Bianchi 46, 23807 Merate, Italy*

P. Giommi, M. Capalbi and F. Tamburelli  
*ASI Science Data Center, via Galileo Galilei, 00044 Frascati, Italy*

L. Angelini  
*NASA/Goddard Space Flight Center, Greenbelt, MD 20071, USA*

G. Cusumano  
*INAF-Istituto di Astrofisica Spaziale e Fisica Cosmica Sezione di Palermo, Via  
 Ugo La Malfa 153, 90146 Palermo, Italy*

H. W. Bräuninger, W. Burkert and G. D. Hartner  
*Max-Planck-Institut für Extraterrestrische Physik, Garching bei München,  
 Germany*

**Abstract.** The *Swift* Gamma-Ray Explorer is designed to make prompt multiwave-length observations of Gamma-Ray Bursts (GRBs) and GRB afterglows. The X-ray Telescope (XRT) enables *Swift* to determine GRB positions with a few arcseconds accuracy within 100 seconds of the burst onset.

The XRT utilizes a mirror set built for JET-X and an *XMM-Newton*/EPIC MOS CCD detector to provide a sensitive broad-band (0.2-10 keV) X-ray imager with effective area of  $> 120 \text{ cm}^2$  at 1.5 keV, field of view of  $23.6 \times 23.6$  arcminutes, and angular resolution of 18 arcseconds (HPD). The detection sensitivity is  $2 \times 10^{-14} \text{ erg cm}^{-2} \text{ s}^{-1}$  in  $10^4$  seconds. The instrument is designed to provide automated source detection and position reporting within 5 seconds of target acquisition. It can also measure the redshifts of GRBs with Fe line emission or other spectral features. The XRT operates in an auto-exposure mode, adjusting the CCD readout mode automatically to optimize the science return for each frame as the source intensity fades. The XRT will measure spectra and lightcurves of the GRB afterglow beginning about a minute after the burst and will follow each burst for days or weeks.

**Keywords:** Gamma-Ray Burst, X-ray telescope, Swift, X-ray instrumentation, X-ray CCD detector, X-ray mirrors

**Abbreviations:** BAT – Burst Alert Telescope; CCD – Charge-Coupled Device; GRB – Gamma-Ray Burst; HPD – Half-Power Diameter; PSF – Point Spread Function; TAM – Telescope Alignment Monitor; TEC – Thermo-Electric Cooler;



TDRSS – Tracking and Data Relay Satellite System; UVOT – Ultra-Violet/Optical Telescope; XRT – X-Ray Telescope

*Dedicated to David J. Watson, in memory of his valuable contributions to this instrument.*

## 1. INTRODUCTION

The *Swift* Gamma Ray Burst Explorer (Gehrels et al., 2004) was chosen in October 1999 as NASA’s next MIDEX mission, and was launched on 20 November 2004. It carries three instruments: a Burst Alert Telescope (BAT; Barthelmy et al., 2004), which identifies gamma-ray bursts (GRBs) and determines their location on the sky to within a few arcminutes; an Ultraviolet/Optical Telescope (UVOT; Roming et al., 2005) with limiting sensitivity of 24<sup>th</sup> magnitude in 1000 s and with 0.3 arcsecond position accuracy; and an X-ray Telescope (XRT). The three instruments combine to make a powerful multiwavelength observatory with the capability of rapid position determinations of GRBs to arc-second accuracy within 1-2 minutes of their discovery, and the ability to measure both lightcurves and redshifts of the bursts and afterglows.

The *Swift* XRT is a sensitive, flexible, autonomous X-ray imaging spectrometer designed to measure fluxes, spectra, and lightcurves of GRBs and afterglows over a wide dynamic range of more than 7 orders of magnitude in flux. The *BeppoSAX* satellite showed that accurate GRB positions can be effectively determined by a good X-ray telescope, since over 84% of GRBs have X-ray afterglows (De Pasquale et al., 2003), compared with about 50% for optical afterglows. However, by the time that *BeppoSAX* was able to observe a typical X-ray afterglow, its intensity had already dropped by 4-5 orders of magnitude (Figure 1).

The *Swift* XRT will begin observations before the GRB ends in some cases, and will fill in the large time gap during which the Lorentz factor of the relativistic blast wave changes from  $\sim 100$  to  $< 10$ . It will provide accurate positions within 5 seconds of target acquisition for typical bursts, allowing ground-based optical telescopes to begin immediate spectroscopic observations of the afterglow.

We previously reported on the instrument design at an early stage in its development (Burrows et al., 2000). Here we describe the final design and performance of the XRT.

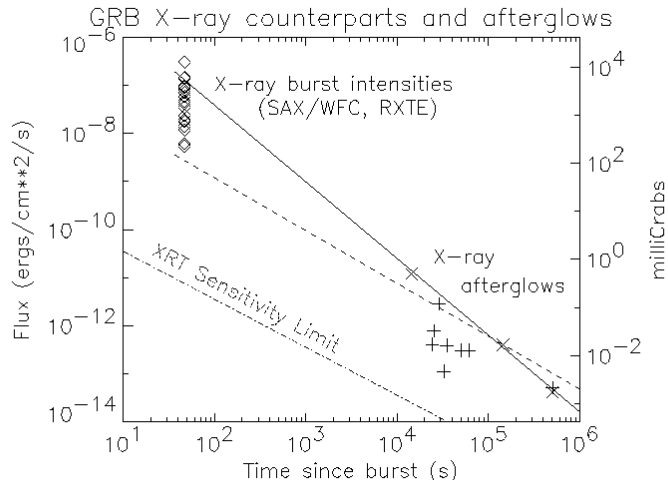


Figure 1. X-ray burst and afterglow lightcurves. The cluster of data points at about 1 minute represents peak X-ray burst fluxes for a number of bursts observed in 1997-1999 by *BeppoSAX* and *RXTE*. The data points between 10<sup>4</sup> and 10<sup>6</sup> s after the burst are *BeppoSAX*, *RXTE*, and *ASCA* afterglow flux measurements for a subset of these bursts. Note the data gap of about 10<sup>4</sup> seconds, during which the afterglow flux drops by about 4 orders of magnitude. The *Swift* XRT will fill in this data gap.

## 2. OVERALL DESCRIPTION

The XRT uses a grazing incidence Wolter I telescope to focus X-rays onto a thermoelectrically cooled CCD. The layout of the instrument is shown in Figures 2 and 3. Figure 4 shows the completed instrument (before thermal blanket installation). A door protects the mirrors during launch. A thermal baffle provides a warm environment for the front end of the mirrors to prevent thermal gradients in the mirror module that could distort the Point Spread Function (PSF). The mirrors are the JET-X flight spares (Citterio et al., 1996; Wells et al., 1992; Wells et al., 1997), and were calibrated at the Panter X-ray Calibration Facility of the Max-Planck-Institute für Extraterrestrische Physik in 1996 (Citterio et al., 1996) and again in July 2000. A composite telescope tube holds the focal plane camera, which contains a single e2v CCD-22 detector. A thermal radiator mounted on the anti-solar side of the spacecraft is coupled to a thermo-electric cooler (TEC) designed to cool the detector to -100 C.

Table I gives the basic design parameters of the XRT. The effective area and sensitivity were verified by an end-to-end X-ray calibration of the assembled instrument at the Panter X-ray Calibration Facility in September 2002.

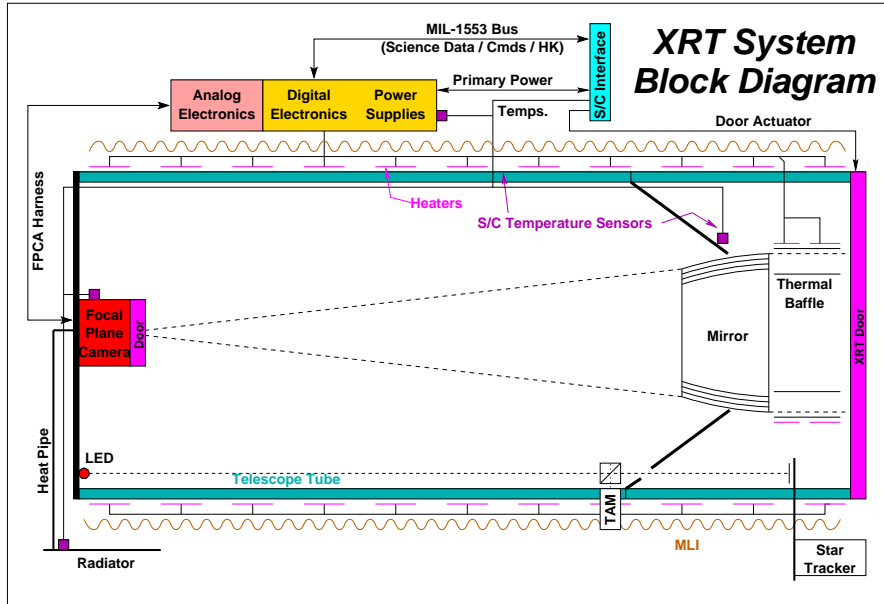


Figure 2. Block diagram of the XRT. The instrument design is described in detail in §4. The TAM is the Telescope Alignment Monitor, an internal alignment monitor described in §4.5.

The design and scientific capabilities of the XRT instrument are summarized in the following sections.

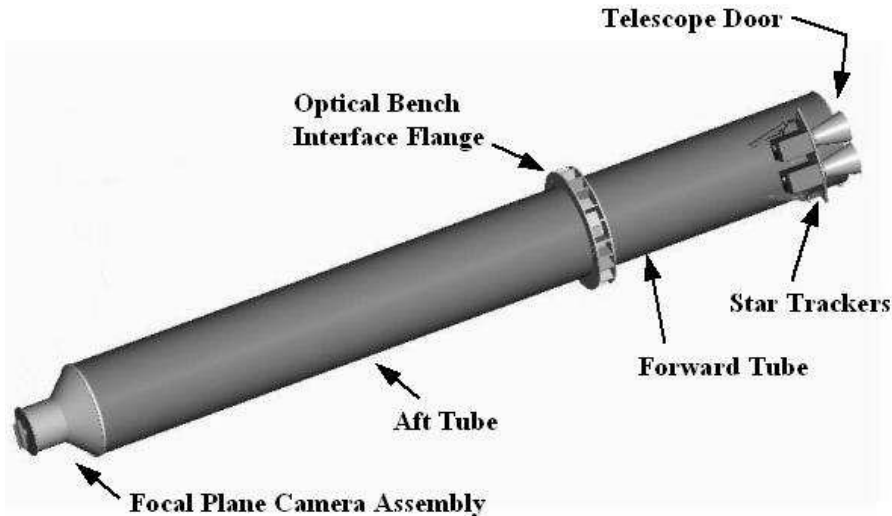


Figure 3. XRT design. The telescope focal length is 3.500m, and the overall instrument length is 4.67m, with a diameter of 0.51m.

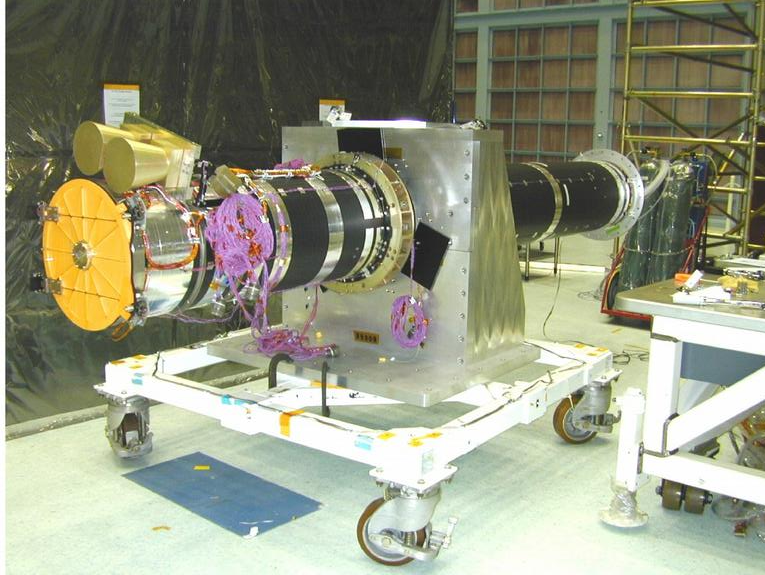


Figure 4. XRT installed in test cart before thermal vacuum tests in July 2002, with star tracker simulators installed. The telescope door is at the left end. The silver bands around the tube are aluminum tape over the operational and survival heaters.

### 3. SCIENCE REQUIREMENTS

There are three primary requirements that drive the design of the XRT: rapid, accurate position determination; moderate resolution spectroscopy; and lightcurves with high timing resolution.

*GRB Position Determination:* The XRT is required to measure afterglow positions with accuracy better than 5 arcseconds within 100 s of a burst alert from the BAT instrument. The spacecraft will slew to the BAT position in 20-75 s, depending on the position of the GRB on the sky. Figure 5 shows a simulated XRT image of a GRB, made using ray-tracing code developed for JET-X and *BeppoSAX* and incorporating the measured PSF of the XRT mirrors. The mirror PSF has a 15 arcsecond Half-Power Diameter (HPD) at the best on-axis focus (at 1.5 keV). It is slightly defocused in the XRT in order to provide a more uniform PSF over the entire field of view, and the instrument PSF is 18 arcseconds (HPD) on-axis at 1.5 keV (Moretti et al., 2004). The centroid of a point source image can be determined to sub-arcsecond accuracy in detector coordinates, given sufficient photons (Hill et al., 2003). Based on *BeppoSAX* and *RXTE* observations of X-ray counterparts of GRBs, we expect that most GRBs observed by *Swift* will have prompt X-ray fluxes of roughly 0.5–5 Crabs in the 0.2–10 keV band

Table I. XRT Instrument Characteristics

Telescope:	Wolter I (3.5 m focal length)
Detector:	e2v CCD-22
Detector Format:	600 × 600 pixels
Pixel Size:	40 μm × 40 μm
Readout Modes:	Image (IM) mode Photodiode (PD) mode Windowed Timing (WT) mode Photon-Counting (PC) mode
Pixel Scale:	2.36 arcseconds/pixel
Field of View:	23.6 × 23.6 arcminutes
PSF:	18 arcseconds HPD @ 1.5 keV 22 arcseconds HPD @ 8.1 keV
Position Accuracy:	3 arcseconds
Time Resolution:	0.14 ms, 1.8 ms, or 2.5 s
Energy Range:	0.2 - 10 keV
Energy Resolution:	140 eV @ 5.9 keV (at launch)
Effective Area:	~ 125 cm <sup>2</sup> @ 1.5 keV ~ 20 cm <sup>2</sup> @ 8.1 keV
Sensitivity:	2 × 10 <sup>-14</sup> erg cm <sup>-2</sup> s <sup>-1</sup> in 10 <sup>4</sup> seconds
Operation:	Autonomous

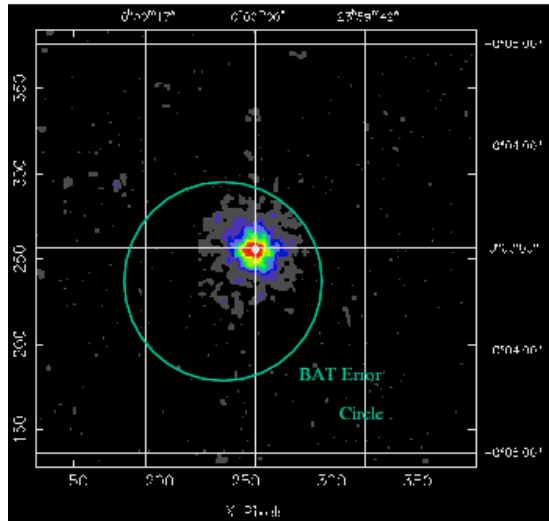


Figure 5. Simulation of a typical XRT early-afterglow observation (about 100s after the burst), using the measured PSF of the XRT mirrors. A 4 arcminute BAT error circle is overlaid for comparison.

(Figure 1). XRT calibration data show that the XRT will obtain source positions accurate to 1-3 arcseconds in detector coordinates for typical afterglows within 5 seconds of target acquisition. When this position is referenced back to the sky, the expected uncertainty is 3-5 arcseconds, due primarily to the alignment uncertainty between the star tracker and the XRT. In order to minimize this error term, the star trackers are mounted on the XRT forward telescope tube (Figures 3, 4), and a Telescope Alignment Monitor (TAM; Hopkinson et al., 2003) measures flexing of the telescope tube with subarcsecond accuracy.

*Spectroscopy:* X-ray spectroscopy can constrain important properties of the GRB/afterglow. In the standard fireball model (Mészáros and Rees, 1997), the GRB is produced by internal shocks in the relativistic fireball and the afterglow is produced by external shocks with the ambient medium. While most of the X-ray luminosity of the afterglows arises from non-thermal synchrotron emission from the external shock, there have been reports of X-ray line emission from GRB afterglows (Piro et al., 2000; Reeves et al., 2002). These may be the result of thermal emission or of X-ray reflection (Lazzati et al., 1999). Observations of the X-ray spectrum may therefore detect emission lines, which can provide direct information on such parameters as the composition and ionization structure of the shocked gas, as well as the redshift of the GRB. Absorption edges from surrounding unshocked gas will be observable over a wide range of column densities (Lazzati et al., 2002), and these edges can also provide both redshift and abundance information.

The XRT energy resolution at launch was about 140 eV at 6 keV (Figure 16), and spectra similar to that shown in Figure 6 will be obtained routinely. The strong Fe emission line in this simulated spectrum ( $E_{rest} = 6.7$  keV) enables a measurement of the redshift that is accurate to about 10%. The XRT transmits unprocessed spectra to the ground through the Tracking and Data Relay Satellite System (TDRSS) within 5–10 minutes of each BAT burst alert to facilitate mission planning and follow-up observations of afterglows with interesting X-ray spectra. [These unprocessed spectra have no event recognition applied and are suitable only for qualitative purposes. Fully processed quick-look science data will be available from the Swift Data Center several hours after each observation for use in scientific analysis.]

The XRT readout modes are designed to allow spectroscopy for sources up to  $\sim 6 \times 10^{-8}$  erg cm $^{-2}$  s $^{-1}$  (0.2–10 keV). Sources brighter than this will be piled up even in the fastest readout mode, but we are developing techniques for analyzing these piled-up data (see §7.5). For more information on XRT readout modes, see Hill et al. (2004).

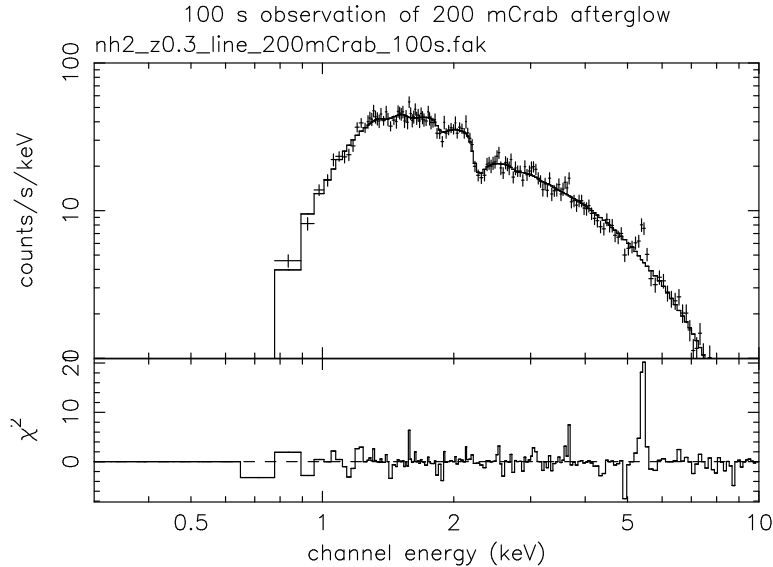


Figure 6. Simulated spectrum from a 100 s XRT observation of a 200 mCrab afterglow at  $z=0.3$ , assuming a power law spectrum plus a redshifted Gaussian Fe line ( $E_{rest} = 6.7$  keV).

*Light Curves:* The XRT is required to provide accurate photometry and light curves with at least 10 ms time resolution. Two timing modes have been implemented to meet this requirement: Photodiode (PD) mode and Windowed-Timing (WT) mode.

Photodiode mode is based on a timing mode originally developed for the JET-X instrument. It provides the best time resolution (0.14 ms), but integrates the count rate over the entire CCD and therefore provides no spatial information. It is suitable for use in uncrowded fields, or fields dominated by a single bright source, and can measure source fluxes as bright as 65 Crabs. Because photodiode mode combines data from the entire CCD, the on-board calibration sources (located over the corners of the CCD; see § 4.3) contaminate PD mode spectra, and it is important to subtract this instrumental background accurately before beginning astrophysical analysis.

Windowed timing (WT) mode is similar to the timing modes available on the *Chandra*/ACIS instrument and the *XMM*/EPIC MOS cameras, and provides about 2 ms time resolution with 1-D spatial resolution within a window 8 arcminutes wide. A more detailed discussion of WT mode is presented in §4.7.

Flux accuracy for light curves has a systematic uncertainty of about 10% for a wide range of incident fluxes up to  $8 \times 10^{-7}$  erg cm $^{-2}$  s $^{-1}$ . Figure 20 shows a light curve from Panter calibration data with the



incident flux ranging over five orders of magnitude. XRT light curves begin as soon as the GRB enters the XRT field of view.

## 4. INSTRUMENT DESCRIPTION

### 4.1. STRUCTURE

The layout of the XRT is shown in Figures 2 and 3. The XRT structure is designed around an aluminum Optical Bench Interface Flange (OBIF), with a forward telescope tube supporting the star trackers and the XRT Door Module and an aft telescope tube supporting the Focal Plane Camera Assembly. The total mass of the XRT, excluding the heat pipe/radiator system, is 198.1 kg.

*Optical Bench Interface Flange:* The OBIF (Figure 11) is the primary structural element of the XRT and is responsible for supporting the forward and aft telescope tubes, the mirror module, the electron deflector, and the TAM optics and camera. It also provides the mounting points to the *Swift* Observatory.

*Telescope Tube:* This 508 mm diameter graphite fiber/cyanate ester tube, manufactured by ATK, is composed of two sections. The carbon fiber layup is designed to minimize the longitudinal coefficient of thermal expansion so that temperature gradients will not adversely affect the alignment or focus. The composite tube is lined internally with an aluminum foil vapor barrier to guard against outgassing of water vapor or epoxy contaminants into the telescope interior. The rear tube supports the Focal Plane Camera Assembly, and incorporates internal optical baffles. The forward telescope tube section encloses the mirrors and supports the door assembly and the star trackers. The internal volume of the telescope tube is vented to space through a baffled vent in the Focal Plane Camera Assembly.

*Door:* The telescope tube is sealed at the forward end for ground operations and launch by a single-shot door assembly built by Starsys, which is designed to protect the X-ray mirrors from contamination. This door was opened about two weeks after launch, which gave the spacecraft time to outgas before the XRT mirrors were exposed to the ambient conditions surrounding the spacecraft.

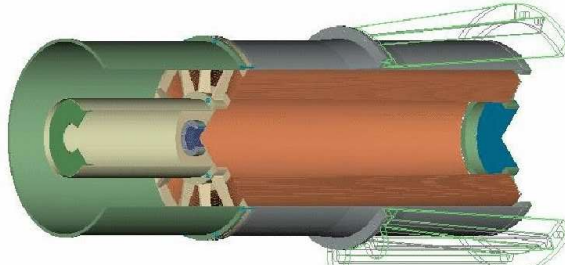


Figure 7. Cutaway view of XRT mirror assembly. The thermal baffle, on the left, consists of two cylinders with foil heaters mounted on them to control the mirror temperature by replacing the heat radiated to space. The mirror module (Fig. 8) is supported by the conical mirror spacer (shown as line drawing for clarity), which attaches it to the optical bench interface flange.

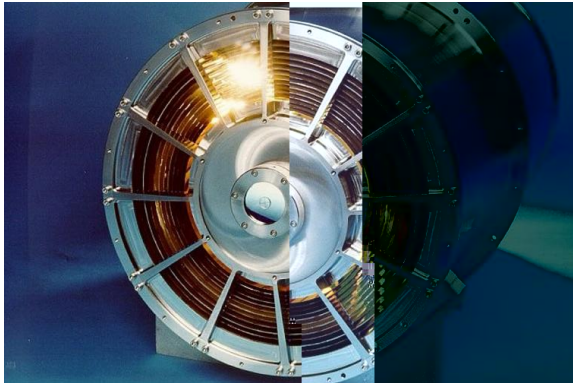


Figure 8. XRT mirror module. This is the FM3 mirror module originally built as a spare mirror set for the JET-X instrument on *Spectrum X- $\Gamma$* . It consists of 12 nested Wolter-I grazing incidence mirrors held in place by front and rear spiders.

## 4.2. OPTICS

*Overall description:* The XRT mirror assembly is shown in Figure 7. It consists of the X-ray mirror module (Figure 8), a thermal baffle mounted in front of the mirrors (to the left in Figure 7), a mirror spacer (shown as a line drawing for clarity) that mates to the XRT optical bench interface flange, and an electron deflector that mounts behind the mirrors (not visible in this figure).

*XRT Mirrors:* The XRT uses the FM3 mirror set (Figure 8) built and calibrated for the JET-X program (Citterio et al., 1996; Wells et al., 1997). The mirror module was developed at the Brera Observatory and was manufactured by Medialario. It has 12 concentric gold-coated

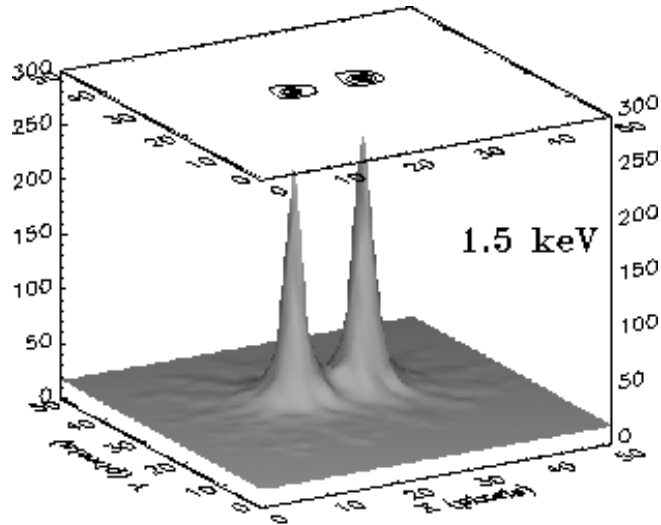


Figure 9. Image of two point sources displaced by 20 arcseconds, made during mirror calibration at the Panter calibration facility. Although the mirror HPD is 18 arcseconds, the PSF is sharply peaked with a FWHM of about 7 arcseconds. The horizontal axes are in pixels and the vertical axis is in arbitrary units.

electroformed Ni shells with focal length 3500 mm. The shells are 600 mm long with diameters ranging from 191 to 300 mm. The effective area and point spread function of the mirrors have been measured for a variety of energies and off-axis angles, and were recalibrated at the Panter facility in July 2000. A calibration image of two sources displaced by 20 arcseconds (Figure 9) shows the very sharply peaked PSF. As noted above, the detector is slightly defocused in the flight instrument in order to optimize the angular resolution over the field of view. Results of the end-to-end calibration of the XRT effective area and PSF are given in Tagliaferri et al. (2004) and Moretti et al. (2004), respectively.

*Thermal Baffle:* A thermal baffle in front of the mirror prevents temperature gradients in the mirror that can distort its figure and degrade its PSF. This system is discussed in more detail in §4.4.

*Electron Deflection Magnets:* The electron flux in our  $584 \times 601$  km,  $20.6^\circ$  inclination orbit will produce a variable detector background. An electron deflector, consisting of a system of 12 rare earth magnets, is installed on the OBIF (Figure 10) just behind the rear face of the mirror module to prevent electrons that pass through the mirror from reaching

the detector. The design is scaled down from the *XMM-Newton* electron deflectors, and has a cutoff energy of 22 keV with near-zero dipole moment.

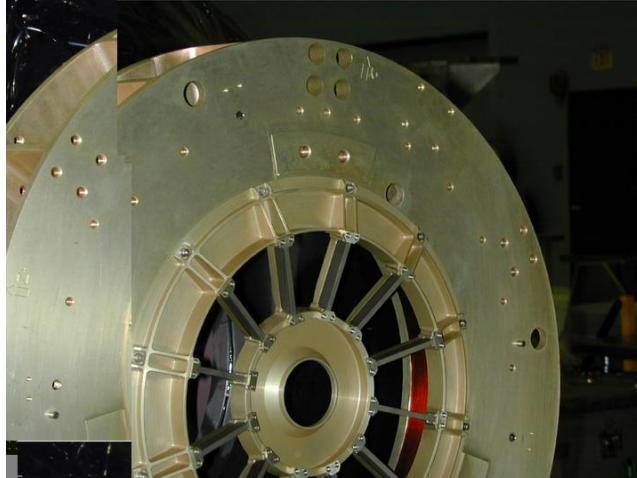


*Figure 10.* The XRT electron deflector, mounted on the rear face of the OBIF. The electron deflector consists of 12 rare earth bar magnets mounted on radial spokes aligned with the mirror spiders. These provide a high azimuthal magnetic field across the optical path with very low dipole moment.

#### 4.3. FOCAL PLANE CAMERA ASSEMBLY (FPCA)

The FPCA (Figures 11 and 12) provides a vacuum enclosure for the CCD and optical blocking filter during ground operations and launch, radiation shielding for the CCD against trapped protons and cosmic rays, and cooling for the detector. The cryostat has a single-shot door mechanism utilizing redundant Starsys actuators.

The cryostat is attached to a conical interface section that mounts onto the rear tube, supports the cryostat door control hardware and radiator interface, and incorporates a baffled venting system. The vent port allows the telescope internal volume to vent during vacuum testing and launch, while preventing scattered light from entering the CCD enclosure.

A novel feature of the FPCA is the sun shutter, which is a safety mechanism designed to autonomously protect the CCD and filter from accidental solar illumination in the event of an attitude control failure. The sun shutter is powered by a Ga-As array mounted at the top of the inner thermal baffle, which provides power to the sun shutter electronics and closes the shutter if the spacecraft slews to within  $\sim 30$  degrees of the Sun, even if the instrument is turned off. The sun shutter can also

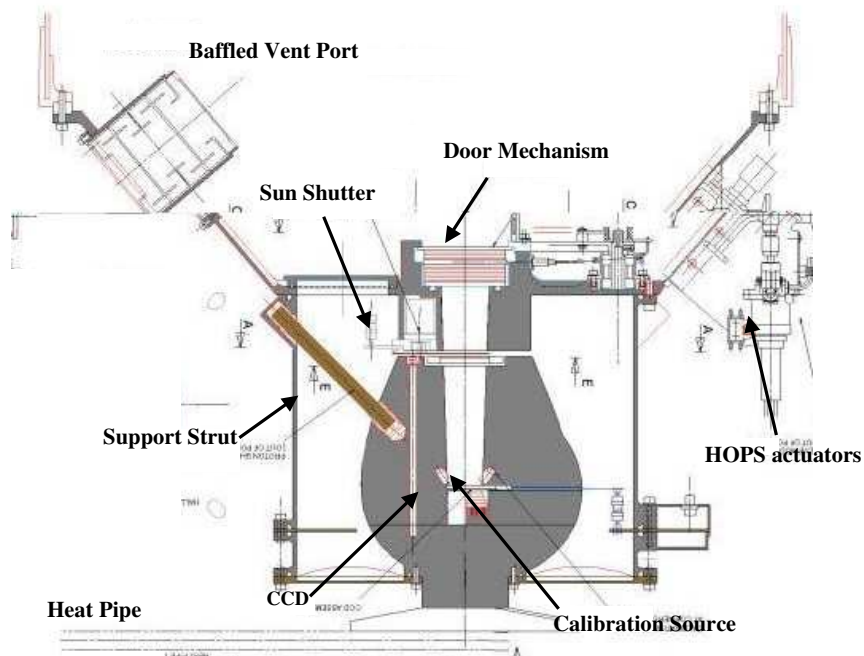


*Figure 11.* Focal Plane Camera Assembly cross-section. The entire proton shield is cooled to a temperature of  $T < -50$  C by the HRS (a radiator/heat pipe system). A TEC integrated into the CCD flight package is designed to maintain the CCD temperature at  $-100$  C, using a closed-loop cooling control system. The FPCA also houses the XRT baffled vent. An autonomous sun shutter protects the detector and filter from accidental exposure to the sun in the event of an attitude control failure. The optical light blocking filter sits immediately below the sun shutter.

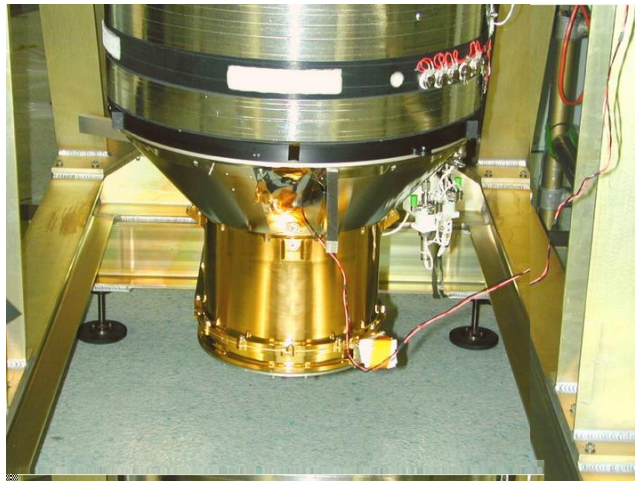


*Figure 12.* The XRT Focal Plane Camera Assembly, mounted on the bottom of the XRT instrument.

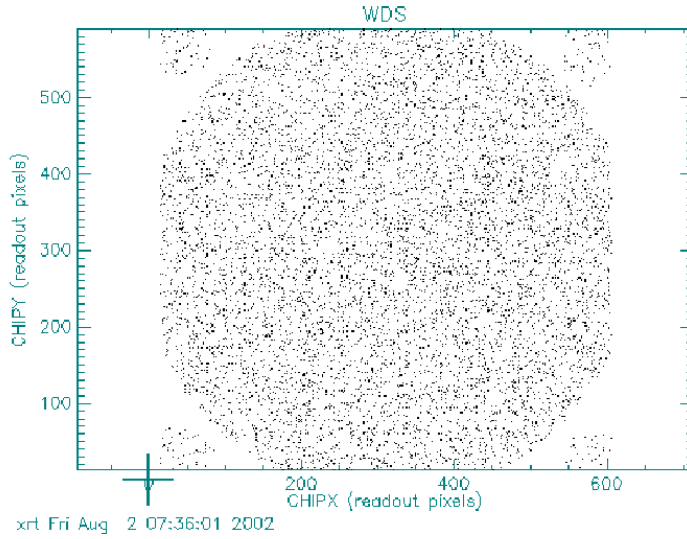


Figure 13. XRT image of the on-board calibration sources. Each spot represents a single X-ray photon. The large central circle shows the instrument field of view illuminated by an  $^{55}\text{Fe}$  calibration source mounted on the inside of the camera door. The four circles of X-rays in the CCD corners are from sources that illuminate the CCD corners continuously during flight.

be opened or closed by telecommand, but it will never be intentionally closed after launch.

The FPCA also houses two sets of  $^{55}\text{Fe}$  calibration sources, which undergo inverse  $\beta$ -decay and produce Mn  $K\alpha$  and  $K\beta$  X-rays at 5.9 and 6.5 keV. An image collected during instrument thermal vacuum testing in July 2002 is shown in Figure 13. The central circular region shows the field of view (FOV) of the instrument (defined by the circular optical blocking filter housing, but slightly truncated by the edges of the CCD), which was illuminated by a bright  $^{55}\text{Fe}$  calibration source located on the inside of the camera door during ground testing and the first three weeks of flight operations. The spectrum of these events is shown in Figure 14. This source was moved out of the FOV when the camera door was opened about three weeks after launch. The four circular clusters of X-ray events in the corners of the detector are the in-flight calibration sources, which permit us to measure resolution, gain, and charge transfer efficiency throughout the mission.

#### 4.3.1. Optical Blocking Filter

A thin Luxel filter is installed in front of the CCD to block optical light. The filter is similar to those used on the *Chandra*/ACIS and *XMM-Newton*/EPIC instruments. It consists of a single fixed polyimide film 1840Å thick, coated on one side with 488Å of aluminum. The optical

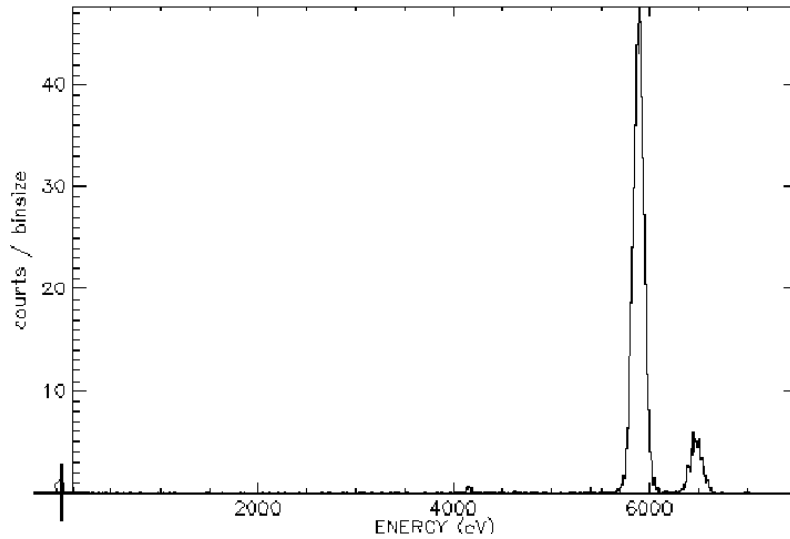


Figure 14. XRT spectrum of Mn  $K\alpha$  and  $K\beta$  X-rays from the door source (PC mode). The FWHM of the 5.9 keV line is 135–140 eV, depending on event grade.

transmission of the filter is about  $2.5 \times 10^{-3}$ . The filter can be seen in the center of Figure 15, which shows the interior of the FPCA. The relatively high filter transmission allows optical light from bright stars to contaminate some fields, and also allows optical light scattered from the bright Earth into the camera when viewing near the Earth limb in daylight. Data cleaning can eliminate both sources of contamination for most directions on the sky.

#### 4.3.2. XRT Detectors

*CCD Architecture:* The CCD-22 detector, designed for the EPIC MOS cameras on *XMM-Newton* by e2v (formerly known as EEV), is a three-phase frame-transfer device, which utilizes high resistivity silicon and an open-electrode structure (Holland et al., 1996) to achieve a useful bandpass of 0.2 to 10 keV (Short et al., 1998). It has an imaging area of  $2.4 \times 2.4$  cm. The image section of each CCD is a  $600 \times 600$  array of  $40\mu\text{m} \times 40\mu\text{m}$  pixels, each pixel corresponding to 2.36 arcseconds in the *Swift* focal plane. The storage region is a  $600 \times 600$  pixel array of  $39\mu\text{m} \times 12\mu\text{m}$  pitch.

*Energy Resolution:* The energy resolution of the CCD-22 is shown in Figure 16, in which the dotted line is the ideal (Fano-limited) resolution, the solid line is the predicted resolution for an EPIC MOS CCD and the points are measurements from a typical flight device.



Figure 15. Interior of the FPCA, showing the lower half of the camera. The circular UV/optical blocking filter in the center of the photo is mounted at the top of the lower proton shield, which is mechanically supported by four fiberglass struts. The black ring around the filter is the filter frame, which defines the instrument field of view. The sun shutter assembly (not shown) mounts immediately above the filter.

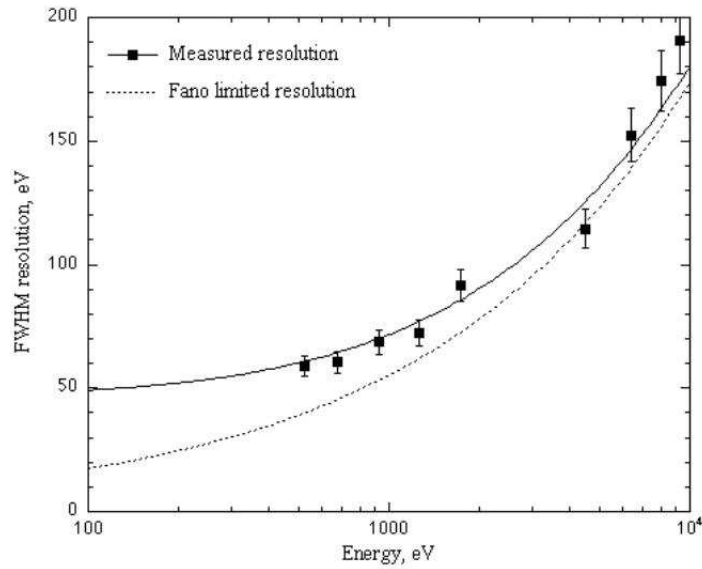


Figure 16. CCD-22 energy resolution above 500 eV.



Below  $\sim 500$  eV the effects of charge trapping and loss to surface states become significant.

*Quantum Efficiency:* The QE of an X-ray CCD is determined at low energies by the gate structure and at high energies by the depletion depth. A special “open-gate” electrode structure gives the CCD-22 excellent low energy quantum efficiency, while high resistivity silicon provides a depletion depth of 30 to  $35\mu\text{m}$  to give good QE at high energies. Quantum efficiency measurements of these detectors have been made at the University of Leicester and at the Orsay Synchrotron. These measurements have been used to validate our Monte Carlo model of the CCD-22 spectral response. The model was used to construct XRT response matrices for all readout modes and for various selections of event grades (Mukerjee et al., 2004).

*Radiation Hardness:* CCDs are susceptible to both ionizing and non-ionizing radiation damage, but the primary area of concern for an X-ray photon-counting CCD spectrometer in low Earth orbit is displacement damage caused by proton irradiation, which results in the creation of electron traps in the silicon lattice. These traps degrade the charge transfer efficiency of the device over time and directly degrade its energy resolution. We note that the ability of the CCD to measure accurate source positions and lightcurves is unaffected by this proton damage until doses far in excess of the total *Swift* mission dose are reached.

We performed a radiation study for the XRT in the baseline *Swift* orbit of 600 km altitude and  $22^\circ$  inclination. This study indicated that the equivalent 10 MeV proton flux seen by the XRT detectors will be  $3.4 \times 10^8$  protons  $\text{cm}^{-2} \text{yr}^{-1}$ . At the actual orbital inclination of  $20.6^\circ$  the dose will be somewhat less. The expected total dose for the XRT in a nominal two-year mission is therefore comparable to the total mission fluence of  $5 \times 10^8$  protons  $\text{cm}^{-2}$  expected for *XMM-Newton*. Considerable analysis and laboratory test data from the EPIC program are therefore directly applicable to the XRT. Laboratory measurements using CCD-22s irradiated to  $2.5 \times 10^8$  10 MeV protons  $\text{cm}^{-2}$  have been used to verify that the XRT will have energy resolution of better than 300 eV at 6 keV after 3 years on-orbit (Short, 2000).

#### 4.4. THERMAL DESIGN

*Cryostat:* The instrument was designed to operate the X-ray CCD detectors at -100 C ensure low dark current and to reduce sensitivity to radiation damage. A failure of the TEC Power Supply shortly after

launch prevents us from reaching this temperature or from maintaining a stable temperature on-orbit. In practice the CCD is now being cooled passively through the HRS to temperatures ranging from about -50C to about -70C, depending on the observatory orientation.

*Heat Rejection System (HRS):* The HRS consists of redundant ethane heat pipes coupled to a 900 cm<sup>2</sup> radiator coated with AZW-LA-II paint. The radiator is carefully configured and integrated with the external spacecraft design to achieve the required low temperature of  $T < -50^{\circ} \text{C}$  in low Earth orbit (depending on orbital parameters and spacecraft orientation). The HRS is connected to the cold finger of the FPCA cryostat, where it provides cooling to the TEC. Although the XRT was not designed for solely passive cooling, the on-orbit performance being achieved meets the design requirements.

*Telescope thermal design:* The XRT uses both passive design features and active thermal control to achieve the high degree of dimensional stability required for arcsecond alignment tolerances. Operational heaters on the telescope tube are controlled by software thermostats in 36 independent zones (arranged in 9 bands, each with four quadrants) to maintain a constant longitudinal thermal gradient and less than 2 C azimuthal thermal gradient on the telescope tube to prevent bending of the tube. Within each quadrant a temperature sensor measures the temperature of that quadrant. These data are monitored by our housekeeping circuits once per second. Every 30 seconds the XRT software compares each quadrant's temperature to an adjustable setpoint for that quadrant and turns the corresponding heater on or off accordingly. The setpoint and deadband (hysteresis) of each quadrant are independently adjustable. This system performed well during thermal balance tests.

Survival heaters are designed to prevent damage to the instrument when the instrument power is off. Survival heaters are located at critical points on the telescope tube and on the electronics box.

*Mirror thermal design:* The mirror module must be maintained at  $18 \text{ C} \pm 0.5 \text{ C}$  with a delta of less than 1 C from front to back in order to prevent degradation of the mirror PSF. The mirrors are not heated directly; instead, an actively controlled thermal baffle in front of the mirrors replaces the heat radiated to space by the mirrors. The baffle consists of an inner cylinder and an outer cylinder with heaters, thermostats, and temperature sensors. The temperature profile of the baffle is actively controlled at two longitudinal locations by pairs of operational control heaters with software thermostats, which balance

the heat lost to space by the mirrors. Thermal control is provided by the flight software using adjustable setpoints in the same way that the operational tube heaters are controlled. During thermal balance tests the flight mirrors were replaced with an identical mirror set with thermal instrumentation, and the mirror baffles successfully maintained the thermal gradient along the mirrors at a few tenths of a degree.

When the instrument is turned off the mirror baffle temperature is maintained by redundant survival heaters controlled by mechanical thermostats. This prevents the mirrors from becoming too cold in the event of an observatory safehold.

#### 4.5. TELESCOPE ALIGNMENT MONITOR (TAM)

Although we expect the composite tube/heater thermal system to provide a stable platform, the XRT will be operating in an unusually dynamic thermal environment, due to the rapid slewing of the observatory. As an additional measure to correct for any thermal variations affecting the instrument alignment, the XRT has an internal Telescope Alignment Monitor (TAM) designed to actively measure any remaining alignment errors between the XRT boresight and the star trackers.

The TAM (Figure 17) uses one of two redundant LEDs mounted on the FPCA, which are observed by a small radiation-hard programmable CMOS active pixel sensor camera developed for space applications by SIRA Electro-Optics. The TAM camera and optics block are mounted on the optical bench interface flange (OBIF), which is the hard mount point for the forward and aft telescope tubes and the mirror module, and which is mounted in turn to the *Swift* optical bench. The TAM camera monitors two light paths: the direct path from the FPCA LED, and a secondary path that includes a reflection from a mirror mounted to the star tracker platform. The direct path monitors lateral motion of the FPCA relative to the OBIF, which defines (to first order) the XRT boresight. The secondary path monitors changes in the tilt of the star trackers relative to the OBIF, and is sensitive to deviations in the star tracker boresight. These two paths produce two images of the LED every five minutes, which are independently monitored and telemetered. The TAM centroids are calculated on-board and are used to calculate GRB positions to be telemetered to the Gamma-ray Coordinate Network (GCN). They are also recorded in the science telemetry stream for use by ground processing software to construct accurate sky maps for the XRT.

We have performed several tests to verify the accuracy and utility of the TAM data. We have measured the displacement of TAM centroid positions as the telescope tube heaters were used to bend the rear tube

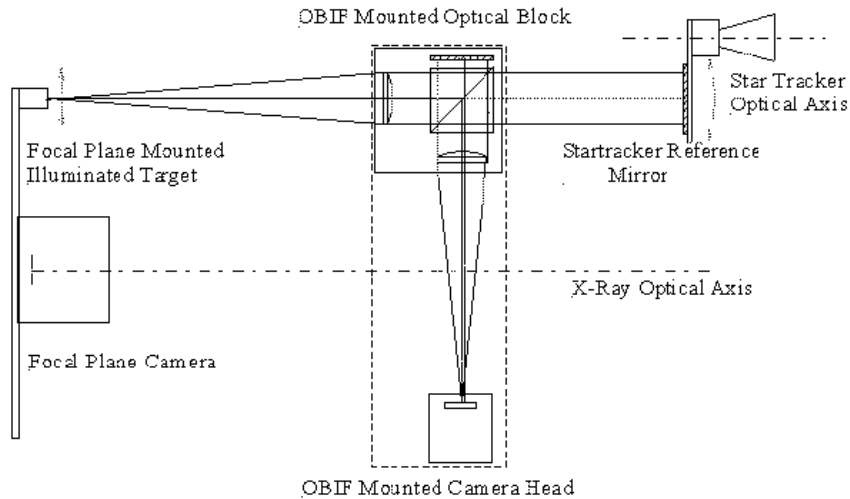


Figure 17. Optical design of the Telescope Alignment Monitor.

slightly by heating it asymmetrically. Movement of the TAM image by less than 0.05 TAM pixels, corresponding to movement of the XRT boresight by less than 0.5 arcseconds, is easily measurable.

#### 4.6. ELECTRONICS DESIGN

The overall electronics design of the XRT is shown in the block diagram in Figure 18. The electronics design has been discussed in some detail previously (Burrows et al., 2000; Hill et al., 2000). The instrument is controlled by a RAD6000 board designed originally for the Mars98 mission. The CCD is controlled by a radiation-hard digital signal processor using software-controlled waveforms, allowing us to implement a very flexible instrument with readout modes optimized to deal with sources ranging over a very wide dynamic range. Dual signal chains extract the CCD signal packets from the detector video signal, using a correlated double sampler.

#### 4.7. AUTOMATED OPERATIONS

Because the *Swift* spacecraft must respond rapidly to new targets, the *Swift* instruments must be able to operate autonomously. This poses interesting new problems for the instrument design. Over the course of a typical GRB observation, the burst/afterglow flux will decrease by many orders of magnitude, and the XRT must be able to observe over this wide dynamic range without detector saturation at early times when the burst and afterglow are bright, while preserving as much

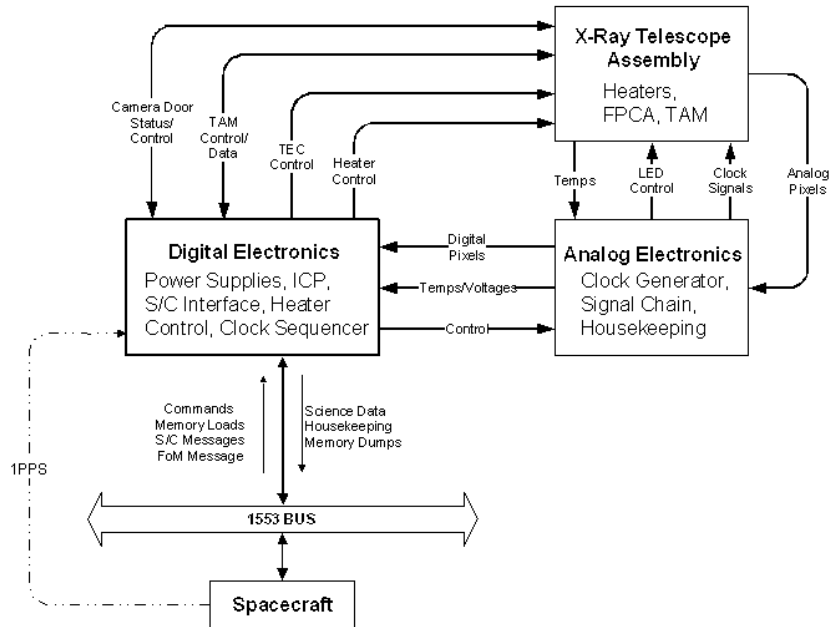


Figure 18. Simplified XRT Electronics Block Diagram.

information about the incident photons as possible during sensitive observations of faint afterglows at later times. The XRT is designed for completely autonomous operation, switching between different readout modes according to the instantaneous count rate in each CCD frame, as shown in Figure 19. This algorithm was successfully tested at the Panter X-ray facility using a variable source flux ranging over five orders of magnitude, designed to mimic the behavior we expect from real GRBs (Figure 20). The autonomous operation of the XRT and its readout modes are described in more detail in Hill et al. (2004). We briefly describe the readout modes here:

**Image (IM) mode:** the CCD is operated like an optical CCD, collecting the accumulated charge from the target and reading it out without any X-ray event recognition. For a typical GRB, this image will be highly piled up and will therefore produce no spectroscopic data, but it will produce an accurate position and a good flux estimate. Image mode is operated with low gain to allow observations up to the full-well capacity of the CCD (in normal gain we are limited by the analog-to-digital converter range). Image mode uses either 0.1 or 2.5 second exposures, depending on the source flux, with the selection made automatically on-board. Image mode can be

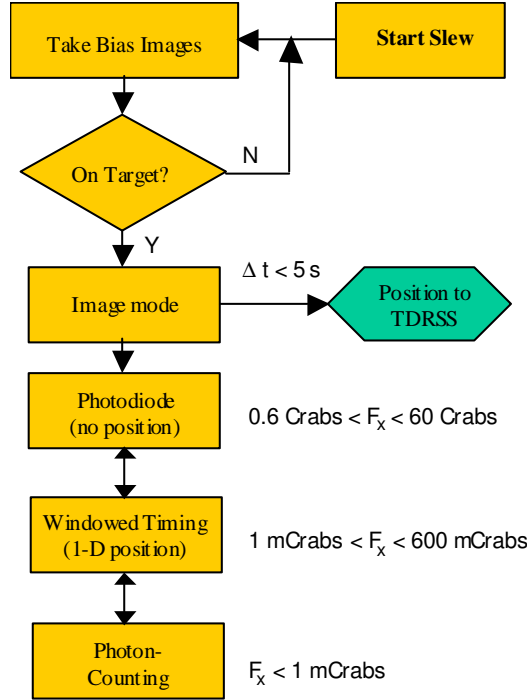


Figure 19. Simplified XRT automation flow chart for a new GRB.

used to determine on-board centroids for source fluxes between 25 mCrabs and at least 45 Crabs. The following data products are produced: the GRB centroid position and X-ray flux estimate, telemetered through TDRSS and distributed immediately to the community through the Gamma-ray burst Coordinate Network (GCN; Barthelmy et al., 2000); a postage-stamp image ( $2' \times 2'$ ), also telemetered via TDRSS and distributed through the GCN; and a compressed image (pixels above a threshold) in the normal science telemetry stream. The X-ray flux estimate assumes a Crab-like spectrum.

Photodiode (PD) mode: a fast timing mode designed to produce accurate timing information for extremely bright sources. This mode alternately clocks the parallel and serial clocks by one pixel each. Charge is accumulated in the serial register during each parallel transfer, with the result that each digitized pixel contains charge integrated from the entire field of view (although not simulta-

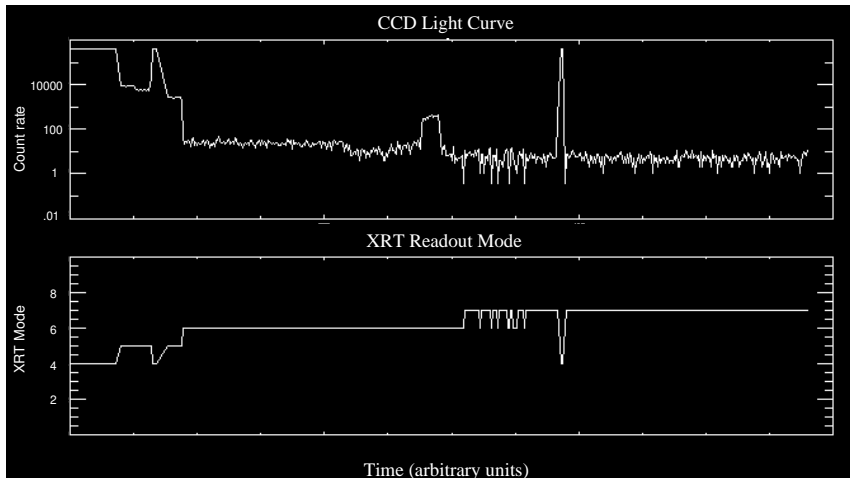


Figure 20. XRT light curve during Panter tests, with incident flux ranging over 5 orders of magnitude. The upper panel shows the XRT lightcurve; the vertical axis is the count rate (log scale), and the horizontal axis is CCD frame number. The lower panel shows the XRT readout mode, which changes automatically in response to changes in the countrate. A value of 4 represents PD mode (high rate), 5=PD mode (low rate), 6=WT mode, and 7=PC mode.

neously). For the GRB case, where we expect the image to be dominated by a single bright source, photodiode mode produces a high-speed light curve with time resolution of about 0.14 ms. This mode is useful for incident fluxes up to 60 Crabs, and has manageable pileup for fluxes below 2 Crabs. Ground-processed data products in photodiode mode are FITS binary table files with the time, energy, and grade (or pattern) of each recorded event (unless the data are too piled-up to identify individual photon events). Event grades for PD mode are described in Figure 21.

Windowed Timing (WT) mode: uses a 200 column window covering the central 8 arcminutes of the FOV (other window sizes are also possible). Imaging information is preserved in one dimension, but the columns are clocked continuously to provide timing information in the trailed image along each column, at the expense of imaging information in this dimension. Pixels are binned by  $10\times$  along columns. This mode has 1.8 ms time resolution for a 200 column window. It is useful for fluxes below 5000 mCrabs, and has minimal pileup below 1000 mCrabs. Ground-processed data products are FITS binary table events files with the 1-D position, arrival time, energy, and pattern of each X-ray event. Event grades for WT mode are described in Figure 21.

## XRT Timing Mode Event Recognition Patterns

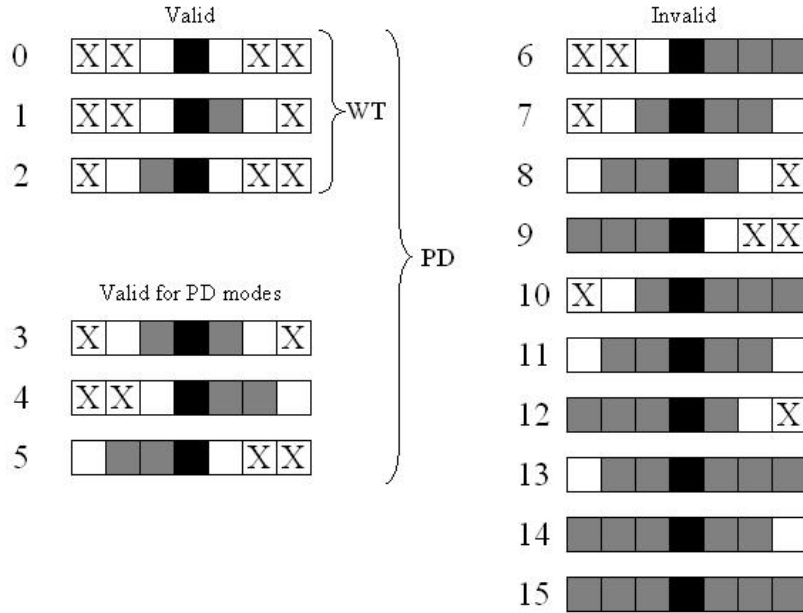
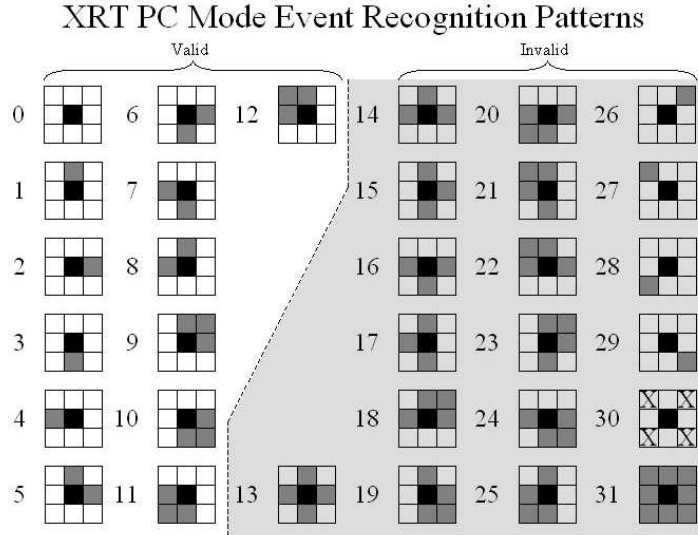


Figure 21. XRT timing mode event grades. For WT mode, only event grades 0-2 represent valid X-ray events. Valid events in PD mode include grades 0-5. In both cases the black pixel represents the local maximum (the pixel containing the most charge), the gray pixels are those with signal levels above the event threshold, and the white pixels are those with signal levels below the event threshold. Pixels containing ‘X’ are those for which the signal level does not matter.

Photon-counting (PC) mode: retains full imaging and spectroscopic resolution, but time resolution is only 2.5 seconds. PC mode uses a “normal” CCD readout sequence, in which the entire CCD is read out every 2.5 seconds, and processed on-board by subtracting a bias map and searching for X-ray events in  $5 \times 5$  pixel “neighborhoods” around each local maximum pixel. It is useful for fluxes below 1 mCrab. Ground-processed data products are FITS binary table events files with the 2-D position, arrival time, energy,  $3 \times 3$  pixel neighborhood centered on the event, and the grade (or pattern) of each event. Grades are recorded using a scheme similar to the *XMM-Newton*/EPIC MOS pattern library. Event grades for PC mode are described in Figure 22 and are assigned during ground processing.





*Figure 22.* XRT Photon-Counting mode event grades. Grades 0-12 represent valid X-ray events, while grades 13-32 represent primarily charged particle background events or piled up events. For each grade, the black pixel represents the local maximum (the pixel containing the most charge), the gray pixels are those with signal levels above the event threshold, and the white pixels are those with signal levels below the event threshold. Pixels containing ‘X’ are those for which the signal level does not matter. Grade 32 (not shown here) is a catch-all for all patterns not specifically defined here.

## 4.8. XRT SOFTWARE

### 4.8.1. *Flight Software*

There are two main pieces of flight software:

- The Instrument Control Processor (ICP; this is the RAD6000 CPU) software is responsible for instrument control, data collection and processing, and spacecraft interfacing. The ICP software is written in C and runs under the VxWorks operating system. On boot-up, the code performs self-tests and enters Manual State with the CCD in Null mode (clocks running but no digitization of the data). Manual state is used for engineering tests, calibration, or instrument configuration. Once commanded into Auto State, the software automatically collects and processes data as described in more detail by Hill et al. (2004). Background processes ingest data from the TAM, perform memory scrubbing, and transmit telemetry data to the spacecraft.

- The Clock Sequencer board produces the CCD clock waveforms using a Motorola 21020 Digital Signal Processor (DSP). Clock waveforms are generated by an IDL program that uses a graphical user interface to produce 21020 DSP assembler code (Hill et al., 2000). The code is then assembled and uploaded to the instrument. On-board waveform programs support a number of readout modes, including diagnostic modes that facilitate checkout of the camera during ground tests and on orbit.

#### 4.8.2. *Ground Processing and Data Analysis Software*

The Swift Data Center (SDC) at NASA/GSFC is responsible for the Level 0 software, which produces time-ordered telemetry data, and for the Level 1 software, which produces standard format FITS event files.

The Level 2/3 software is called the XRT Data Analysis Software (*XRTDAS*). It consists of a set of FTOOLS specifically developed for the XRT instrument by the ASI Science Data Center (ASDC, Frascati, Italy) in collaboration with the HEASARC at NASA/GSFC. *XRTDAS* processes the FITS-formatted Level 1 XRT telemetry data and generates higher-level scientific data products, including cleaned and calibrated event files, images, spectra and light curves. The *XRTDAS* input and output files are in FITS format and fully comply with the NASA/GSFC Office of Guest Investigator Programs FITS standard conventions.

*XRTDAS* is written using the C, Fortran and Perl languages. It uses the HEASARC calibration database (CALDB) mechanism, and runs on most popular Unix platforms. *XRTDAS* is part of the HEASoft Swift package for the analysis of all *Swift* data and is distributed by the HEASARC (<http://heasarc.gsfc.nasa.gov>). This distribution includes full documentation for *XRTDAS*.

The SDC is also responsible for the standard automated data processing pipeline of the *Swift* ground system, which is routinely run on all *Swift* data. The output of the pipeline is a standard set of data products that are archived and made publicly available by the on-line services of the HEASARC at NASA/GSFC, the Italian Swift Archive Center (ISAC, operated jointly by the ASDC and OAB), and the UK Swift Science Data Centre (UKSSDC) at the University of Leicester. *XRTDAS* can also be used to reprocess low level archival XRT data to apply non-standard screening or filtering criteria, or to take into account changes in the calibration files.

*XRTDAS* supports the processing of all XRT readout modes. The main steps of the XRT standard data processing pipeline are summarized below. In addition, *XRTDAS* includes a number of tasks, such as

centroid determination and exposure map calculation that are not used in the standard pipeline.

Steps common to all XRT science readout modes:

- Correction of the spacecraft attitude file using the information obtained with the Telescope Alignment Monitor (TAM)
- Generation of a filter file containing instrument housekeeping, attitude and orbit-related parameters values, to be used for the calculation of the time intervals where the events are considered acceptable for science data analysis (Good Time Intervals, or GTI).

Steps specific to Image Mode processing:

- Bias subtraction, removal of calibration sources and of bad pixels.
- Calculation of an image in sky coordinates using spacecraft attitude and telescope alignment.

Steps specific to Photon Counting mode:

- Assignment of XRT Grade for the 3x3 charge distribution matrix (see Figure 22) and calculation of PHA values. (Bias subtraction in PC mode is performed on-board.)
- Gain correction for Charge Transfer Inefficiency (CTI) to convert X-ray PHA values into Pulse Invariant (PI) energies.
- Transformation from raw to sky coordinates using spacecraft attitude and the telescope alignment.
- Flagging and screening of events associated with the calibration sources, and with bad, hot or flickering pixels.
- Selection of events based on grade and good time intervals.
- Creation of high-level science products (e.g. spectra, lightcurves and images).

Steps specific to timing modes (Windowed Timing and Photodiode modes):

- Assignment of the photon arrival time based on CCD photon position. For the case of Photodiode modes all photons are assumed to come from the target of the observation.
- Flagging of partially exposed and piled-up frames and bias subtraction when not done on board (Photodiode modes only).

- Event recognition using a 7x1 pixel array, grade assignment (see Figure 21), and PHA calculation.
- Gain correction for Charge Transfer Inefficiency (CTI).
- For Windowed Timing mode, which has one-dimension imaging capability, transformation from raw detector to sky coordinates using spacecraft attitude and the telescope alignment. For Photodiode mode, which has no imaging capability, only detector coordinates are calculated.
- Flagging and screening for events associated with bad columns (Windowed Timing mode only).
- Selection of events based on grade and Good Time Intervals.
- Creation of high-level science products (e.g. spectra, lightcurves and images) from the screened event file. Since no position information is available in Photodiode mode, no spatial filtering is applied in this case.

Images and spectra obtained through TDRSS messages can also be processed with *XRTDAS*. In this case images can be displayed in sky coordinates, source fluxes can be estimated and data files can be converted from their telemetry format into FITS files usable with standard imaging and spectral analysis packages.

## 5. XRT OPERATIONS

With the exception of occasional manual calibration observations, the operation of the XRT is completely autonomous and is driven by the response of the observatory to its on-board observation timeline and to newly discovered GRBs. The *Swift* Mission Operations Center (MOC) will load pre-planned target (PPT) timelines onto the observatory on a daily basis or as needed. New GRBs trigger Automated Targets (ATs), which are generated on-board by the BAT instrument. A software process called the Figure of Merit process controls the observing timeline and arbitrates between PPTs and ATs according to their assigned observing priorities.

Because the *Swift* observatory is in low Earth orbit, and because the two Narrow-Field Instruments (XRT and UVOT) cannot be pointed closer than 30 degrees to the Earth’s limb, there is no “Continuous Viewing Zone” for *Swift*, and all observations will be broken up by observing constraint violations that require the spacecraft to slew to

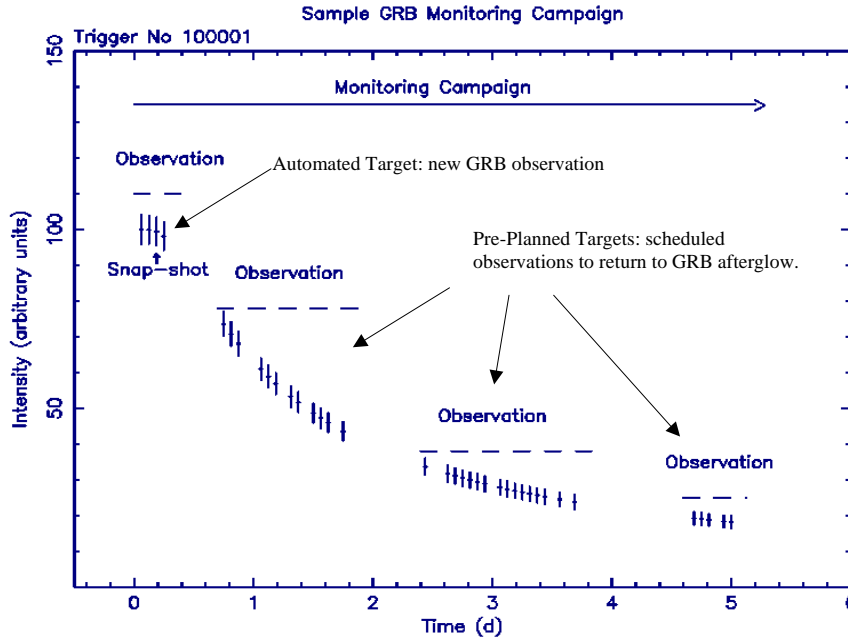


Figure 23. Typical *Swift* observing program for a new GRB. The observing program is broken into several “observation segments” (labelled “observations” on the figure), each lasting 1-2 days, which are in turn broken into “snapshots” of typical duration 20-30 minutes. The first observation segment is scheduled automatically on-board and lasts 60,000 s (on-target). Subsequent observation segments are pre-planned on the ground as updates to the mission timeline.

a new target. This results in observations of any given target that are broken into segments of (typically) 20-30 minutes duration, which we refer to as “snapshots”, with other objects intervening. This is illustrated graphically in Figure 23. Snapshots are grouped together into “observation segments” that cover several days. A single roll angle will be used for each observation segment. In ground processing, each observation segment is processed as a single data set.

## 6. ALIGNMENT

### 6.1. GROUND ALIGNMENT

The telescope optical pointing direction or boresight was established by using a micro-alignment telescope (MAT) mounted on a special alignment jig to accurately measure the line from the center of the CCD through the center of the mirror module. The measured boresight was transferred to an external alignment reference cube, using optical

transfer flats and an additional autocollimator. Following alignment, this master alignment cube defines the XRT instrument axes, with the X-axis parallel to the XRT boresight (+X towards the target), the Y-axis parallel to the CCD serial register, and +Z in the CCD parallel readout direction.

## 6.2. ON-ORBIT ALIGNMENT

On-orbit alignment was accomplished through a two-step process. In the first step, the instrument was pointed at several bright stars. The positions of the stars were measured in both the XRT (by optical light leak through the blocking filter) and the star tracker images, and the star tracker software parameters were updated to zero out the boresight alignment so that the star tracker reports its orientation with respect to the XRT boresight. Secondary alignment measurements were made by the XRT, and XRT instrument software parameters were adjusted to zero out residual offsets to the Star Tracker coordinate system. We expect on-orbit alignment to be accurate to within 2 arcseconds.

## 7. CALIBRATION

The XRT flight detector and optical blocking filter were calibrated at the University of Leicester. The mirrors were calibrated at the Panter X-ray Calibration Facility operated by MPE in Neuried, Germany. End-to-end testing and calibration of the fully assembled instrument was also performed at the Panter facility in September 2002. This end-to-end calibration verified the instrument point spread function, effective area, and focus. Results of these calibrations have been reported elsewhere (Moretti et al., 2004; Tagliaferri et al., 2004; Mukerjee et al., 2004) and are incorporated in the XRT response matrices, which are available from the Swift Science Center at NASA/Goddard Space Flight Center (<http://swiftsc.gsfc.nasa.gov/docs/swift/swiftsc.html>).

### 7.1. CCD SELECTION AND CALIBRATION

Four *Swift*/XRT CCDs were tested, characterized, and calibrated at the University of Leicester. The UL X-ray calibration facility uses a Kevex source and fluorescent targets, plus an electron-bombardment source with coated anodes and a monochromator, to generate X-ray emission lines from Boron  $K\alpha$  (183 eV) to Arsenic  $K\alpha$  (10532 eV). At energies below 1500 eV, a crystal monochromator is used to isolate the desired emission line. The CCD being tested is mounted on a liquid nitrogen cold finger, and its temperature may be controlled in the range -40 to

-140 C. The X-ray beam flux is monitored with a calibrated lithium drifted silicon detector to measure quantum efficiency.

Selection of potential flight devices was based upon cosmetic defects (bright and dark pixels and columns), spectral resolution across the energy band, quantum efficiency and spatial uniformity of the low energy response. One flight detector and three spare devices were calibrated over a range of energies, temperatures and flux rates, with nearly a million photons collected on the flight CCD (Beardmore et al., 2005). The calibration data were used to tune our Monte Carlo CCD model, and response matrices have been generated for all XRT readout modes (Mukerjee et al., 2004; Mukerjee et al., 2005).

## 7.2. MIRRORS

The flight mirrors were calibrated at the Panter X-ray Calibration Facility operated by MPE in Neuried, Germany as part of the JET-X calibration in 1996 (Citterio et al., 1996) and were stored at the Osservatorio Astronomico di Brera in a dry, inert atmosphere in a hermetically sealed shipping container for the next four years. They were recalibrated in July 2000 at the Panter facility to check for any changes in performance since the original calibration. Analysis of these data confirmed the previous results.

## 7.3. END-TO-END CALIBRATION

The end-to-end calibration concentrated on four primary measurements:

*Verification of the focus of the telescope:* The XRT has a fixed focus. An important part of the end-to-end calibration was verification that this focus is accurate within the 1 mm depth of field of the optics. A spacer was installed between the aft telescope tube and the FPCA in order to compensate for the finite source distance. The calibration data verified that the instrument is properly focused (see Figure 24).

*Point-Spread Function:* Measurement of the on-axis and off-axis PSF of the telescope at several energies verified that the mirror mounting has not introduced any distortion to the mirrors. Composite images made from these data are shown in Figure 24. These data were fitted to an analytical model that provides an excellent approximation of the PSF of the telescope as a function of energy and off-axis angle. For details, we refer the reader to Moretti et al. (2004).

*Effective Area:* We measured the end-to-end effective area of the XRT at several energies and off-axis angles. These data were used to derive

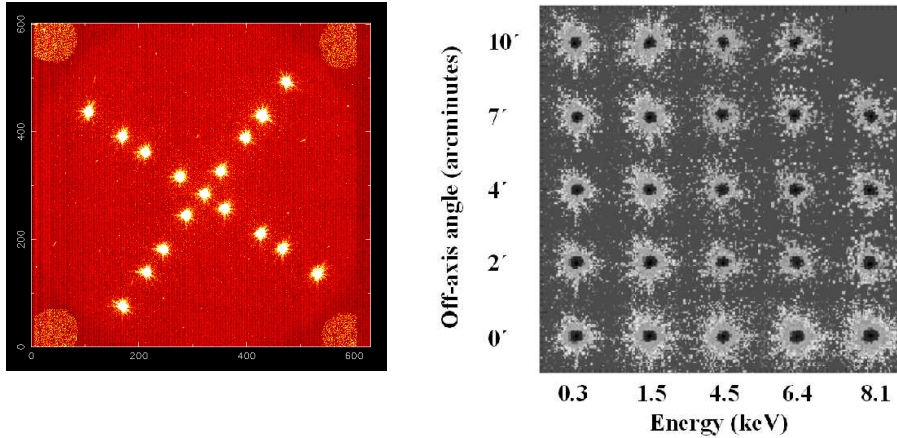


*Figure 24. Left:* Composite of 1.49 keV calibration images taken at Panter at a variety of off-axis angles spanning the XRT field of view. The image quality is quite uniform over the entire field of view. The large, diffuse circles in the corners of the detector are the on-board calibration sources. The dark band on the right-hand side of the image is the over-clocked pixels, which are used to measure the baseline level. **Right:** composite images made at five different energies and five off-axis angles. The PSF degrades significantly at high energies due to increased scattering from the mirror surfaces, but still retains a sharp core.

on-axis effective area curves and vignetting functions for all of the XRT readout modes (Tagliaferri et al., 2004). The results have been incorporated into an ancillary response file generator program, *mkarf*, that creates an appropriate effective area curve (ARF file) for each observation.

#### 7.4. IN-FLIGHT CALIBRATION

In-flight calibrations have been performed during the Performance Verification phase following instrument turn-on, and will continue as an ongoing activity. The PV phase calibration includes the following:

- Calibration of the XRT PSF as a function of off-axis angle, using bright X-ray point sources with hard and soft spectra (PKS 0312-770, RX J0720.4-3125, GX1+4, RXS J1708-4009).
- Calibration of the end-to-end instrument effective area, using supernova remnants with well-known and constant spectra (Crab, Cas A, 2E0102-7217).
- Calibration of the energy response using bright emission line sources (2E0102-7217, Cas A, AB Dor, HD 35850, Capella).



- Calibration of the timing modes using X-ray pulsars (RXS J1708-4009, Crab), cross-calibrated to RXTE.
- Special calibrations include determination of off-axis stray light sensitivity, optical blocking filter transmission, boresight alignment, and centroiding accuracy.

These calibration observations will be repeated on a periodic basis (roughly once every six months) to monitor any instrument changes with time.

In addition to calibration with astrophysical sources, the XRT will be calibrated on an ongoing basis using four small on-board  $^{55}\text{Fe}$  sources that constantly illuminate the corners of the CCD at a low rate. These events (which are outside the instrument field of view) are tracked as part of our trend analysis to monitor energy resolution, gain, and charge transfer efficiency throughout the mission.

Finally, full CCD images are sent to the ground on a regular basis to monitor the detector for any changes in hot pixels or other artifacts that could affect the on-board event processing. On-board lists of bad rows, columns, or pixels will be updated based on analysis of these images by the instrument team.

## 7.5. PILE-UP

The automated operating modes of the XRT are designed to minimize pileup for most observations. Photon pileup should be minimal for source fluxes below 1 Crab. However, the earliest observations of the brightest GRB afterglows may occur while the source flux is more than 10 times brighter than this, and these early data may be significantly piled-up. Two strategies have been developed to cope with pileup in these cases:

*Photodiode Mode:* Pileup in PD mode data will occur for source fluxes in excess of  $\sim 6 \times 10^{-8} \text{ erg cm}^{-2} \text{ s}^{-1}$ . Because pileup changes the electron distribution in the detector, it is accompanied by a loss of information and cannot be directly corrected. We are modelling the effects of pileup for PD mode in order to produce algorithms designed to allow the user to obtain approximate spectral parameters, even in the event of severe pileup, following the technique described for piled-up *Chandra* observations of the Crab nebula by Mori et al. (2004).

*Windowed Timing Mode:* In WT mode the CCD is clocked continuously in the parallel shift direction, so that an image made from these data consists of a vertical streak across the CCD. Pileup in WT mode

results in a piled-up central streak, surrounded on both sides by lower count rates resulting from the wings of the PSF. Very bright sources with severe pile-up can be analyzed in WT mode by utilizing only the wings of the PSF. The XRT *mkarf* program can produce the special ARF files required for this type of analysis.

### Acknowledgements

This work is supported at Penn State by NASA contract NAS5-00136; at the University of Leicester by the Particle Physics and Astronomy Research Council on grant number PPA/G/S/00524; and at INAF-OAB by funding from ASI on grant number I/R/309/02. We gratefully acknowledge the contributions of dozens of members of the XRT team at PSU, UL, OAB, GSFC, and our subcontractors, who helped make this instrument possible.

### References

- Barthelmy, S. et al.: 2000, ‘GRB Coordinates Network (GCN): A Status Report’, in *Gamma-Ray Bursts*, eds. R. M. Kippen, R. S. Mallozzi and G. J. Fishman, p. 731, AIP, New York
- Barthelmy, S. et al.: 2004, *Proc. SPIE* **Vol. No. 5165**, pp. 175–189
- Beardmore, A. et al.: 2005, *Nucl. Instr. & Methods*, in preparation
- Burrows, D. N. et al.: 2000, ‘The Swift X-ray Telescope’, *Proc. SPIE* **Vol. No. 4140**, pp. 64–75
- Citterio, O., et al.: 1996, ‘Characteristics of the flight model optics for the JET-X telescope onboard the SPECTRUM X- $\Gamma$  satellite’, *Proc. SPIE* **Vol. No. 2805**, pp. 56–65
- De Pasquale, M. et al.: 2003, ‘A Comparative Study of the X-ray Afterglow Properties of Optically Bright and Dark Gamma-Ray Bursts’, *Astrophys. J.* **Vol. No. 592**, pp. 1018–1024
- Gehrels, N. et al.: 2004, ‘The Swift Gamma-Ray Burst Mission’, *Astrophys. J.* **Vol. No. 611**, pp. 1105–1120
- Hill, J. et al.: 2000, ‘Laboratory X-ray CCD Camera Electronics - a test bed for the Swift X-ray Telescope’, *Proc. SPIE* **Vol. No. 4140**, pp. 87–98
- Hill, J. et al.: 2003, ‘An Algorithm for Locating PSF-Like Events and Computing the Centroid in X-ray Images’, *Proc. SPIE* **Vol. No. 4851**, pp. 1347–1355
- Hill, J. et al.: 2004, ‘Readout Modes and Automated Operation of the Swift X-ray Telescope’, *Proc. SPIE* **Vol. No. 5165**, pp. 217–231
- Holland, A. D., Turner, M. J. L., Abbey, A. F., and Pool, P. J.: 1996, ‘MOS CCDs for the EPIC on XMM’, *Proc. SPIE* **Vol. No. 2808**, pp. 414–420
- Hopkinson, G. R., Purll, D. J., Abbey, A. F., Short, A., Watson, D. J. Wells, A.: 2003, ‘Active pixel array devices in space mission’, *NIMA* **Vol. No. 513**, pp. 327–331
- Lazzati, D., Campana, S., and Ghisellini, G.: 1999, ‘Iron line in the afterglow: a key to unveil gamma-ray burst progenitors’, *MNRAS* **Vol. No. 304**, pp. L31–L35

- Lazzati, D., Covino, S., and Ghisellini, G.: 2002, ‘On the role of extinction in failed gamma-ray burst optical/infrared afterglows’, *MNRAS* **Vol. No. 330**, pp. 583–590
- Mészáros, P., and Rees, M. J.: 1997, ‘Optical and Long-Wavelength Afterglow from Gamma-Ray Bursts’, *Astrophys. J.* **Vol. No. 476**, pp. 232–237
- Moretti, A. et al.: 2004, ‘Swift XRT Point Spread Function measured at the Panter end-to-end tests’, *Proc. SPIE* **Vol. No. 5165**, pp. 232–240
- Mori, K., Burrows, D. N., Hester, J. J., Pavlov, G. G., Shibata, S., and Tsunemi, H.: 2004, ‘Spatial Variation of the X-ray Spectrum of the Crab Nebula’, *Astrophys. J.* **Vol. No. 609**, pp. 186–193
- Mukerjee, K. et al.: 2004, ‘The Spectroscopic Performance of the Swift X-ray telescope for gamma-ray burst afterglow studies’, *Proc. SPIE* **Vol. No. 5165**, pp. 251–261
- Mukerjee, K. et al.: 2005, *Astron. and Astrophys.*, in preparation
- Piro, L. et al.: 2000, ‘Observation of X-ray Lines from a Gamma-Ray Burst (GRB 991216): Evidence of Moving Ejecta from the Progenitor’, *Science* **Vol. No. 290**, pp. 955–958
- Reeves, J. et al.: 2002, ‘The Signature of Supernova Ejecta in the X-ray Afterglow of the  $\gamma$ -ray Burst 011211’, *Nature* **Vol. no. 416**, pp. 512–515
- Roming, P. et al.: 2005, ‘The Swift Ultra-Violet/Optical Telescope’, *Space Science Reviews*, in press
- Short, A. D. T.: 2000, ‘Swift XRT: proton environment and CCD degradation’, report *XRT-LUX-RE-001*, Space Research Centre, University of Leicester
- Short, A. D. T., Keay, A., and Turner, M. J. L.: 1998, ‘Performance of the XMM EPIC MOS CCD Detectors’, *Proc. SPIE* **Vol. No. 3445**, pp. 13–27
- Tagliaferri, G. et al.: 2004, ‘Swift XRT Effective Area measured at the Panter end-to-end tests’, *Proc. SPIE* **Vol. No. 5165**, pp. 241–250
- Wells, A. et al.: 1992, ‘The JET-X Instrument for the USSR Spectrum RG Mission’, *Proc. SPIE* **Vol. No. 1546**, pp. 205–220
- Wells, A. et al.: 1997, ‘X-ray Imaging Performance of the Flight Model JET-X Telescope’, *Proc. SPIE* **Vol. No. 3114**, pp. 392–403
- Address for Offprints:* David Burrows, 2582 Gateway Dr., State College, PA 16801 USA

